Modeling the Lateral Wet Oxidation of $Al_xGa_{1-x}As$ into Arbitrary Mesa Geometries

K. Alfaro-Bittner,[1] R.G. Rojas,[1] G. Lafleur,[2] S. Calvez,[2] G. Almuneau,[2] M.G. Clerc,[3] and S. Barbay[4,*]

[1] *Instituto de Física, Pontificia Universidad Católica de Valparaíso, Casilla 4059, Valparaíso, Chile*

[2] *LAAS-CNRS, Université de Toulouse, CNRS, Toulouse, France*

[3] *Departamento de Física and Millenium Institute for Research in Optics, Facultad de Ciencias Físicas y Matemáticas, Universidad de Chile, Santiago, Chile*

[4] *Centre de Nanosciences et de Nanotechnologies, CNRS, Univ. Paris-Sud, Université Paris-Saclay, Palaiseau, France*

(Received 12 July 2018; revised manuscript received 8 January 2019; published 22 April 2019; corrected 30 April 2019)

We report experimental and theoretical results on the lateral wet oxidation of bidimensional thin aluminum-rich layers into AlOx. We introduce a reaction-diffusion model of oxidation front propagation that includes effects of anisotropies and compare it to experimental results. This model can be used with any starting geometry, possibly nonconvex, and is deduced from the chemical reactions of wet oxidation of $Al_xGa_{1-x}As$ -based layers. Numerical simulations performed with simple and complex geometries are in excellent agreement with the experimental observations. Our method is general and can apply to other oxides. It opens the way to the fine control of wet-oxidation fronts and to the formation of AlOx layers with a desired geometry that has numerous practical and relevant applications for, e.g., waveguiding or carrier confinement in photonics.

DOI: 10.1103/PhysRevApplied.11.044067

I. INTRODUCTION

The wet oxidation of aluminum rich layers is of prime importance for the manufacturing of electrical injected vertical-cavity surface-emitting lasers (VCSELs) [1–4], but also in many other areas in photonics [5], such as, e.g., to easily fabricate low-loss waveguides [6]. This technique is commonly used in VCSELs for current and optical confinement [7]. The wet selective oxidation of aluminum-rich layers produces an oxide (AlOx), which has a low refractive index, is transparent from visible to infrared wavelengths, and is an electrical isolator. Technically, the wet oxidation is obtained by inserting an $Al_xGa_{1-x}As$ material with a high aluminum content (typically $x > 0.9$) in a furnace saturated with water vapor at a high temperature of the order of 400 °C. If the Al-rich layer is thin and sandwiched between two layers with low Al content, oxidation of a mesa can proceed from the etched borders and progress in time essentially along the layer plane, as a two-dimensional process [8]. Water vapor reacts with the Al-rich layer to form a stable porous oxide [9]. For a thin aluminum-rich layer surrounded by Ga-rich layers, we can consider that there is no three-dimensional effect and the oxidation front that is produced forms a clear edge separating the oxidized material from the unoxidized one. This edge is called an oxidation front in the following. The front can progress in the structure thanks to the oxide porosity that allows for oxidant (water vapor) and volatile by-products (arsenic, arsine) to pass through. Interestingly, the wet oxidation process is not an isotropic process and the speed of the oxidation front depends on the crystallographic orientation, as shown in Refs. [10] and [11]. With present-day techniques, current apertures with micron-size diameters can be obtained, but they are difficult to control and to manipulate [12]. A better control can be achieved with an optical *in situ* monitoring [13]. Especially, it is difficult to ensure a perfectly circular shape, or any other given shape, that would, e.g., allow us in a VCSEL to control the polarization state of the emitted light [14–16] and fine-tune or select the emission mode [17]. Also, submicron-size apertures may be desirable to obtain high-quality factor microcavities [18] or for selective current injection of a single quantum emitter [19–21]. It is thus essential to understand and to be able to model the wet oxidation process in its dynamical and geometrical aspects.

II. LATERAL WET OXIDATION

The problem of the dynamics of wet oxidation of Al-rich thin layers has been tackled in several works [12,22,23]. Most models assume either planar or circular oxidation

*sylvain.barbay@c2n.upsaclay.fr

geometries disregarding any anisotropies. It is worth noting that the initial mesa shape has a strong influence on the oxidation kinetics. Indeed, circular fronts with small radii of curvatures have larger velocities than planar ones, in a nontrivial way. A method able to predict the oxidation front dynamics with anisotropic front velocities has been developed [24] in the case of mesas with convex polygon shapes (possibly having a large number of facets, thus giving rise to smooth edges) but is limited to specific geometries. A method applicable to any geometry and able to include effects of oxidation anisotropies is missing. This is the subject of this paper, in which we will present our approach to this issue. Contrary to the model developed in Ref. [12], we do not aim at calculating an equation for the front position directly. Instead, we consider the reaction-diffusion dynamics of a two-dimensional field corresponding to the water vapor concentration in which we include an anisotropic reaction term. Also, the reaction term is a nonlinear term in our case and is deduced from the chemical model of wet oxidation considered. This term, which includes the chemical reactions' kinetics, determines together with the field shape itself the front propagation dynamics, in contrast with many other approaches where the front speed is an external parameter. As such, the method applies to any kind of initial geometry and is valid as long as the oxidation process can be considered as a two-dimensional one, i.e., for not-too-thick aluminum-rich layers. The model is described below and is compared to experimental results. Examples of complex initial geometries are given to demonstrate the powerfulness of our approach.

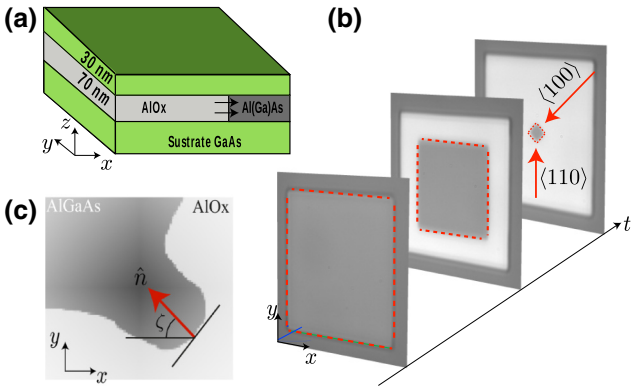

FIG. 1. Lateral wet thermal oxidation of $Al_xGa_{1-x}As$ to AlOx. (a) Schematic representation of AlOx front propagation in a mesa containing an aluminum-rich layer. (b) Sequence of experimental images taken from the top of the mesa at different times. The dark gray and light gray regions account, respectively, for AlAs and AlOx. The dashed line (red) indicates the front interface. (c) Schematic representation of intrinsic coordinates, where $\hat{n}(s)$ is the normal vector to the interface, $\zeta(s)$ is the angle between $\hat{n}$ and the horizontal axis, and s is the arch element coordinate.

The experimental data are obtained from a sample grown by molecular beam epitaxy on a (100) GaAs wafer [cf. Figs. 1(a)–1(c)]. The vertical structure includes a 70-nm-thick AlAs layer capped by a 30-nm GaAs layer. We realize a photolithography masking step to define the studied square-shape mesas, followed by a dry etching down to below the AlAs layer. The sample is then oxidized in a furnace equipped with an *in situ* infrared reflectometry imaging system, allowing us to monitor the time-dependent evolution of the oxidation front with a spatial resolution of 0.8 μm. The sample is oxidized in conditions leading to anisotropic oxidation [11], more precisely, using a reduced-pressure (0.5 atm) environment, a substrate temperature of 400 °C, and a mixed H_2, N_2 and H_2O gas steam generated by an evaporator-mixer system operating at 95 °C.

III. THEORETICAL DESCRIPTION

The wet oxidation process corresponds to the propagation of the oxidized state over the nonoxidized one in a thin film. Both As_2O_3 and As are present as intermediates in the wet oxidation process of AlAs. Their presence can be explained by the chemical reactions [25]

$$\begin{aligned} 2AlAs + 6H_2O &\rightleftharpoons Al_2O_3 + As_2O_3 + 6H_2, \\ As_2O_3 + 3H_2 &\rightleftharpoons 2As + 3H_2O, \\ As_2O_3 + 6H &\rightleftharpoons 2As + 3H_2O. \end{aligned} \tag{1}$$

As can be seen, the presence of water vapor is fundamental for the propagation of the oxidation. Most importantly, one can see from inspection of the set of Eq. (1) that water is a catalyst in the process of wet oxidation. Hence, we introduce the water vapor concentration $u(\vec{r}, t)$, where t and $\vec{r}(x, y)$ account for time and the horizontal coordinates, respectively. The role of mass transport of other compounds has already been studied in this context in Refs. [25–27] and is neglected here in the first approximation. First, we consider that the wet oxidation process is isotropic. From the chemical reactions (1), the water vapor concentration satisfies the reaction-diffusion partial differential equation [28]

$$\partial_t u = u^3 \left(K_1 - K_2 u^3\right) + D\nabla^2 u, \tag{2}$$

where K_1 and K_2 are the rate constants of creation and destruction of water vapor, respectively, which involve the collision cross section of the required molecules times the probability for the reaction. D is the diffusion coefficient.

A. Characterization of stability properties of the states

The reaction-diffusion model described by Eq. (2) has two homogeneous equilibria: $u \equiv u_0 = 0$ and $u \equiv u_s = (K_1/K_2)^{1/3}$. The stability of these homogeneous equilibria

can be intuitively demonstrated by rewriting Eq. (2) as follows:

$$\partial_t u = -\frac{\delta \mathcal{F}}{\delta u}, \tag{3}$$

where the Lyapunov functional $\mathcal{F}$ has the form $\mathcal{F} = \int [V(u) + (\nabla u)^2/2]\, dxdy$. This Lyapunov functional $\mathcal{F}$ corresponds to a free energy for Eq. (2), where $V(u) \equiv -u^4/4 + u^7/7$ is the potential energy and the last term of the free energy accounts for the spatial coupling. Figure 2(a) depicts the potential $V(u)$, where u_0 and u_s are respectively a local maximum and a local minimum. Indeed, these states correspond to an unstable or a stable state, respectively. In the experimental context, the stable equilibrium corresponds to the stable phase (the oxidized material, AlOx), while the unstable one corresponds to the unstable phase (the aluminum-rich material). Note that, for simplicity, we only consider the stoichiometric reaction leading to the formation of Al_2O_3. There can exist fronts connecting these two phases [see Figs. 2(b) and 2(c)] whose dynamics is entirely governed by Eq. (2), with the necessary initial and boundary conditions. The front interface position $\vec{r}_p$ is characterized by $u(\vec{r}_p, t) = u_i \equiv (K_1/K_2)^{1/3}/2$ and has a width given by the square root of the diffusion coefficient ($\sqrt{D}$); see Figs. 2(c) and 2(d). A front that connects a stable and an unstable uniform state is usually called a Fisher-Kolmogorov-Petrosvky-Piskunov (FKPP) front [29–31]. The front propagates from the stable state toward the unstable one [32]. One of the main features of these fronts is that their propagating speed is not unique, but determined by the initial conditions. When the initial condition is bounded, and after a transient state, the front propagates with a definite speed [29,31,32]. The reaction-diffusion Eq. (2) exhibits pushed FKPP fronts [32]; hence, there is no general method to derive an analytic expression for the front speed. We therefore rely on numerical simulations. Figure 2 shows an example of a front propagation in the isotropic case as described by Eq. (2). All numerical simulations are conducted using either a fourth-order Runge-Kutta method in time and a finite difference in space or with a split-operator, spectral method [33]. To compare the experimental and numerical contours, we scale the numerical simulation time, matching the first and the last experimental and numerical contour with a similar shape.

For a large mesa, the front speed goes asymptotically to a constant that depends on the local curvature of the front [34]. When fronts propagate, they end up making the oxidized contour interfaces smoother. Starting from a square interface, as a result of the effect of curvature, the front evolves to a circular shape [cf. Fig. 2(d)]. However, the dynamics previously described is not concordant with that observed experimentally, because the oxidation process must include the oxidation rate anisotropy [11] depending

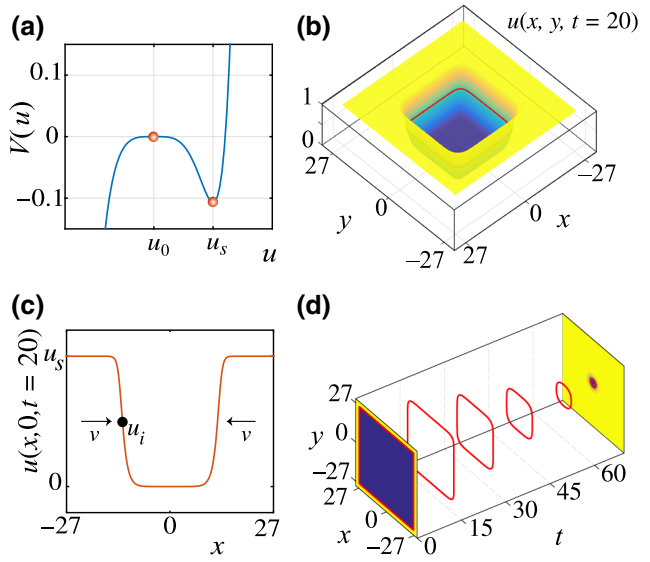

FIG. 2. Front propagation in the reaction diffusion model, Eq. (2), with $K_1 = K_2 = 1$ and $D = 1.0$. (a) Potential of the free energy $\mathcal{F}$ of the model in Eq. (2). u_0 and u_s account for the unstable and stable equilibria. (b) Two- and (c) one-dimensional profile of water vapor concentration $u(\vec{r}, t)$ at a given time. (d) Temporal sequence of the evolution of the interface characterized by $u = u_i$ (red).

on the front orientation relative to the [110] and [100] crystallographic orientations, respectively [cf. Fig. 1(b)].

B. Anisotropic front propagation

To take this effect into account, we modify the nonlinear term in Eq. (2) by

$$\partial_t u = u^3(K_1 - K_2 u^3)[1 + b \sin^2(2\zeta)] + D\nabla^2 u, \tag{4}$$

where $\zeta \equiv \arctan(\partial_x u/\partial_y u)$ is the local angle in intrinsic coordinates between the normal to the interface and the horizontal axis [see Fig. 1(c)] and b is a small parameter that accounts for the strength of anisotropy [24]. If $b > 0$, then the front speed is larger for the [100] direction, whereas if $b < 0$, then it is larger for the [110] direction. According to the sign of b, we call the Ox (respectively Oy) orientation the slow axis and the $\pi/4$ tilted axis with respect to the slow axis is the fast axis. For a nonzero anisotropy, the shape of the oxidation contour can evolve from a square to a diamond as the front propagates [11]. Figure 3 shows the evolution of the interface for the anisotropic model. Depending on the initial condition, we can observe different geometric evolutions of the interface. From the experimental data, we can extract the evolution of the interface. Figure 3(a) shows a direct comparison between the experimental and the numerical oxidation front progression for three different orientations and measuring the distance of the front r to the center of the

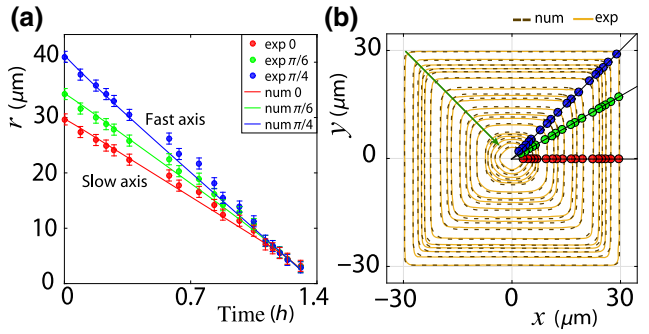

FIG. 3. Oxidation front propagation in the experiment and in the anisotropic model with $K_1 = K_2 = 1$, $b = 0.4$, and $D = 0.0777$. (a) Front dynamics in the experiment (dots) and in the model (solid line) along the slow, fast ($\pi/4$ tilted), and $\pi/6$ tilted axis. The radius r is taken from the center of the mesa. (b) Best matches between experimental and numerical oxidation fronts. The green arrow indicates the temporal evolution. The dots correspond to the experimental points for the three different orientations.

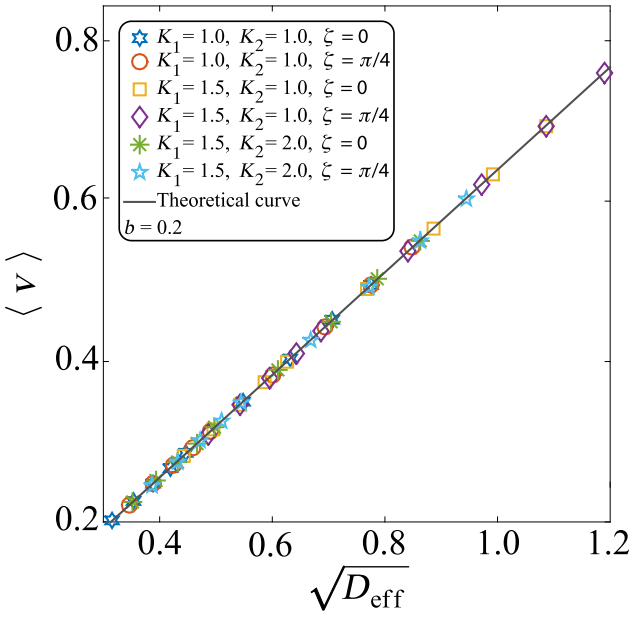

FIG. 4. Comparison between numerical simulations of the flat front mean speed with anisotropy, according to different parameters $K1$, $K2$ and orientations ζ. All the points collapse to the line defined by $v = a\sqrt{D_{\text{eff}}}$, taking $a \approx 0.64$.

mesa. The agreement is satisfactory given the experimental uncertainties. In Fig. 3(b), we display for the overall contour of the oxidized mesa the best matches between the numerical simulations and the experimental observations and they show excellent agreement.

From the theoretical point of view and as previously mentioned, the analytic formula for the front speed of a flat pushed front is generally not possible to obtain. Dimensional analysis is a simple strategy to obtain a functional formula for the front speed v [35]. Starting with the dimension of $[u] = ML^{-3}$ and $[D] = L^2T^{-1}$, we deduce by dimensional analysis that $[K_1] = L^6T^{-1}M^{-2}$ and $[K_2] = L^{15}T^{-1}M^{-5}$, b being a dimensionless parameter. Introducing the parameter $k \equiv [1 + b\sin^2(2\zeta)](K_1^5/K_2^2)^{1/3}$, which has dimensions of the inverse of time ($[k] = T^{-1}$), one can build a unique quantity with D and k having dimensions of speed: $[v] = a\sqrt{kD} = a\sqrt{D_{\text{eff}}}$, where a is a constant to be determined and $D_{\text{eff}} \equiv D[1 + b\sin^2(2\zeta)](K_1^5/K_2^2)^{1/3}$. Without loss of generality, we can choose $\zeta = 0$ and $\zeta = \pi/4$ for the slow and the fast axis. The parameter a can be determined by fitting with the previous formula the speed observed numerically for different parameter settings (cf. Fig. 4). Note that the different numerical values of front speed collapse on a single curve described by $v = a\sqrt{D_{\text{eff}}}$ with $a \approx 0.64$, in good agreement with the dimensional analysis.

One of the interesting technological questions related to the problem of wet oxidation in planar structures is to know whether one can predict the evolution of the oxidation interface for arbitrary initial conditions. Figure 5 shows the interface evolution for a complex photonic structure displaying a ring resonator coupled to a waveguide [36]. Oxidation of the complex geometry induces at the same time inward and outward fronts and includes sharp edges. The qualitative agreement between theory and experiment is again very good. We point out that our approach allows us to characterize front break-ups, as illustrated in Fig. 5, or front disappearance, in contrast to other approaches only considering the advection front dynamics and not the evolution of a whole field (here, water vapor concentration).

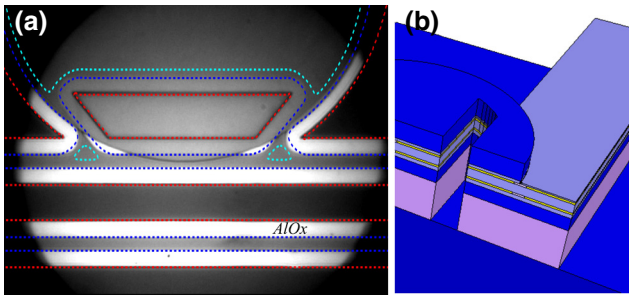

FIG. 5. Front propagation for a complex geometry. (a) Experimental image of the oxidized structure as seen from the top: substrate (dark gray), planar mesa with an $Al_{0.98}Ga_{0.02}As$ layer (medium gray), and aluminium oxide (light gray). The lighter spot corresponds to the microscope-illuminated area. The numerical simulation uses $b = 0.2$, $K1 = K2 = 1$, $D = 0.005$. The initial contour is shown with experimental and numerical results (dashed red). The contours after $t = 7.8$ and $t = 10.8$ are shown in dashed blue and cyan, respectively. (b) Three-dimensional view of the structure. The aluminum-rich layers are in yellow and sandwiched between Ga-rich layers. The horizontal waveguides are 36 μm in width.

IV. TARGET SHAPE: INVERSE FRONT PROPAGATION

A key problem from the point of view of applications (e.g., the fine control of oxidation apertures in VCSELs) is to know whether is it possible to find the starting mesa shape that will evolve, after a given time of oxidation, toward a target shape. The dynamics of front propagation is not reversible in time since any bounded initial condition relaxes to the same front solution. Indeed, the front is an attractive nonlinear wave [32]. The dynamics described by the reaction-diffusion equations (2) and (4) is of an irreversible nature, as one would expect for such a physicochemical process. Figure 6(a) shows the temporal evolution of water vapor concentration for the one-dimensional model equivalent to Eq. (2), given a small perturbation of the water vapor concentration at the edge of the mesa as an initial condition. This initial condition accounts for the launch of the oxidation process from the unstable phase. At time $t = 0$, the water vapor concentration is zero inside the material, except for a small and local perturbation near $x = 0$. As time increases, the front starts to form and then to propagate inside the material to be oxidized. Notice that the front initially accelerates until it reaches an asymptotic speed as illustrated in Fig. 6(b). We can calculate the typical time of the transient to be $\tau_t \sim (K_2^2/3K_1^5)^{1/3}$. This time is effectively quite short and corresponds to the initial stage of the oxidation. During this time, the front advances only a distance of the order of the front width, as can be seen in Fig. 6(a). In real experiments, this would correspond to a distance of a fraction of a micrometer. The dashed curve in the spatiotemporal diagram in Fig. 7 accounts for the asymptotic interface trajectory. In order to study the evolution toward the past of the front, one can use the temporal reversibility

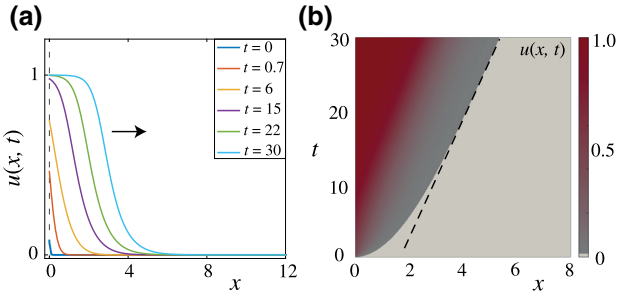

FIG. 6. Numerical simulations of front propagation in one-dimensional model Eq. (4) at the beginning of the oxidizing process with $b = 0.4$, $\zeta = \pi/4$, $K_1 = K_2 = 1$, and $D = 0.0777$. (a) Temporal evolution of the water vapor concentration profile with a small perturbation in the left side of the mesa as an initial condition, $u(x = 0, t = 0) = 0.1$ and $u(x \neq 0, t = 0) = 0$. (b) Spatiotemporal propagation of the water vapor concentration. The dashed line indicates the asymptotic trajectory, in which the front has reached its stationary behavior.

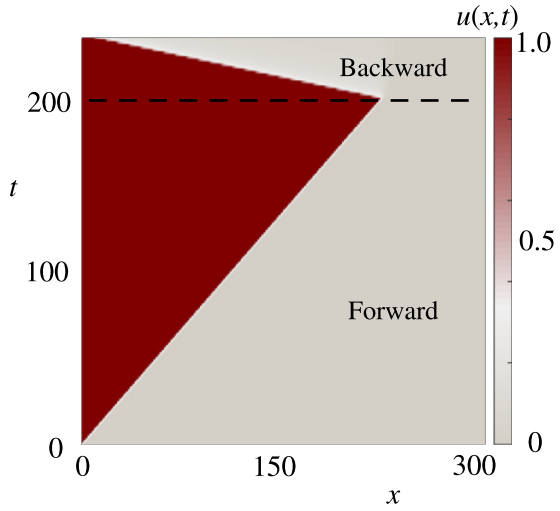

FIG. 7. Forward and backward spatiotemporal evolution of the water vapor concentration of the model in Eq. (4) in one dimension, when one applies the temporal inversion $t \to -t$ and $D \to -D$ at time 200. This numerical simulation considers $b = 0.4$, $\zeta = \pi/4, K_1 = K_2 = 1$, and $D = 0.0777$ for the one-dimensional approach of Eq. (4).

transformation $t \to -t$ and $D \to -D$. The latter operation corresponds to reverting the oxide into the semiconductor material or equivalently considering the inverse chemical reaction of Eq. (1), but keeping the normal diffusion. Figure 7 illustrates how the temporal evolution is modified when one makes the temporal inversion. Numerically, one observes that essentially the direction of propagation of the front is reversed. Nevertheless, the system does not return to its initial condition. Note that the evolution governed by this time-reversed transformation is different from an oxidation process in the opposite direction, which only depends on the initial conditions (e.g., starting with a hole in an unoxidized material vs starting with a mesa). Also, notice that the speeds of forward and backward front propagation are different.

In two dimensions, the problem to find the shape that the mesa should have to achieve a final target shape of the oxide—the inverse problem—is even more complex. In addition to the effects of transients due to the mesa initial condition and to the nonreversibility of the dynamics when the front kinetics is reversed, as we illustrate in the one-dimensional case, there are curvature effects that come into play. To illustrate the complexity of the inverse problem, let us consider the final target shape obtained from a square mesa as an initial condition (at time t_1) for the reversed evolution of Eq. (4) as displayed in Fig. 8. The mesalike initial condition is defined by an abrupt transition across the interface between the nonoxidized (unstable) phase with $u = 0$ and air (absence of material) with $u = u_s/2 = 0.5$. This latter boundary evolves quickly toward the stable phase since it cannot oxidize. After oxidation

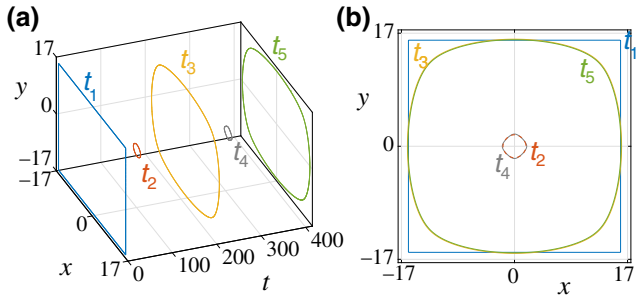

FIG. 8. Temporal evolution of the forward and backward oxidation process in the anisotropic model of Eq. (4) with $K1 = K2 = 1$, $b = 0.4$, and $D = 0.05$. (a) Three-dimensional representation of the contour evolution of the water concentration $u(x, y, t)$. Forward oxidation from t_1 to t_2 and t_3 to t_4. Backward propagation from t_2 to t_3 and t_4 to t_5. (b) Two-dimensional plot for the contour at the respective instants t_1, t_2, t_3, t_4, and t_5. (c) Real-time representation of (a) for the water vapor concentration front.

and at time t_2, we obtain an interface shape (target) in the form of a rounded diamond. Subsequently, we perform the temporal inversion transformation starting from the reversed mesalike initial condition with the diamond shape (t_2) and let the system evolve (backward) up to having an interface area of the order of the original mesa (t_3). Note that the shape found for the interface at time t_3 is close to a square but with rounded, or soft, vertices. This result is reminiscent of the fact that oxidation is an irreversible, memoryless process that tends to wash out any sharp edges due to the effect of nonlinear diffusion. Now, one can consider the square mesa with a rounded vertices interface with the mesalike initial condition (t_3) for the evolution of model Eq. (4) with normal evolution. After propagation of the front (t_4), we find a final interface shape similar to the target shape obtained at t_2. The diamond-shaped interface found at t_4 has slightly sharper edges than the one found at t_2 but both look alike. Even more, repeating the process of temporal inversion, one obtains an interface shape at t_5

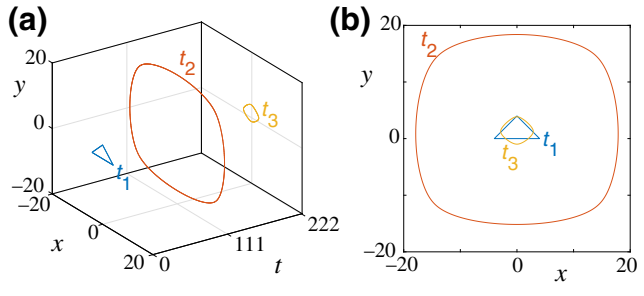

FIG. 9. Same simulation as in Fig. 8 but starting from a triangular mesa as initial condition. (a) Temporal evolution of the time-reversed process from t_1 to t_2 and of the normal oxidation process from t_2 to t_3. (b) Comparison of the front interface shapes obtained at times t_1, t_2, and t_3.

that is close to the one found at t_3. Therefore, different initial mesas evolve to similar interface shapes. The above may be understood as a result of the fact that the diamond shape is the attractor of the system; i.e., any initial condition evolving after a sufficiently long time will always converge to a diamond shape, and an arbitrary target is forbidden. The diamond interface shape results from the crystallographic anisotropy, i.e., the $[1 + b\sin^2(2\zeta)]$ contribution in the model and from the oxidation chemistry under study. To illustrate the latter effect, let us consider an initial (target) interface with a triangular shape (see Fig. 9) that we evolve with the time-reversed process and then forward again. In the initial stage of the reverse evolution (t_1 to t_2), the front relaxes and then propagates outward, losing memory of the initial shape. After a normal evolution, from t_2 to t_3, the final interface shape [cf. Fig. 9(b)] is, this time, significantly different from the target profile because the system has evolved toward its attractor, a diamond shape here, and because the target shape's sharp edges are harder to obtain since they are rounded by the reverse (or normal) evolution. This example illustrate that, for long oxidation times, the inverse problem only exhibits a tractable solution if the target shape is on the path to its attractor shape. Reaching a substantially different target shape at a nonzero evolution time is, however, deemed to be achievable as long as the oxidation time is taken to be sufficiently short (or equivalently, the mesa shape is close to the target shape) to limit the edge-rounding effects induced by the diffusion nonlinearity and the geometric influence of the attractor.

V. CONCLUSION

In conclusion, we introduce a simple model based on physicochemical processes to describe the evolution of planar oxidation fronts in arbitrary two-dimensional geometries with anisotropies, which agrees well with experiments even in the case of complex, nonconvex starting mesas. This model is expected to be valid also for other alloy compositions provided the parameters K_1, K_2, and b are adjusted to match the new oxidation kinetics. The present study can also be applied to the oxidation of other materials if, in addition to the kinetic parameters, one also adjusts the nonlinear part of Eq. (4) to match the oxidation chemistry. Likewise, we study the reversibility of the oxidation process and show how the system consistently evolves toward its attractor after a sufficiently long evolution time. Unsurprisingly, the process of oxidation is not reversible and so is our model. However, we show that some target interface shapes can be obtained with different starting conditions. The obtention of specific target oxidation interface shapes is not always possible if the inverse problem has two many constraints. In the case where a solution exists, it may require either a trial-and-error

approach or necessitate the use of more refined numerical techniques.

ACKNOWLEDGMENTS

M.G.C. and R.G.R. acknowledge the financial support of FONDECYT projects Grants No. 1180903 and No. 1130622, respectively. K.A.-B. is supported by CONICYT, scholarship Beca Doctorado 2014 Nacional No. 21140668. G.L., S.C., and G.A. acknowledge the support by the LAAS-CNRS micro- and nanotechnologies platform, a member of the French RENATECH network, and by the University Paul Sabatier for G.L.'s Ph.D. scholarship.

[1] D. L. Huffaker, D. G. Deppe, K. Kumar, and T. J. Rogers, Native-oxide defined ring contact for low threshold vertical-cavity lasers, Appl. Phys. Lett. **65**, 97 (1994).

[2] D. G. Deppe, D. L. Huffaker, and T. H. Oh, in *CLEO 97, Summaries of Papers Presented at the Conference on Lasers and Electro-Optics* (IEEE, Baltimore, MD, USA, 1997).

[3] K. D. Choquette, K. L. Lear, R. P. Schneider, K. M. Geib, J. J. Figiel, and R. Hull, Fabrication and performance of selectively oxidized vertical-cavity lasers, IEEE Photon. Technol. Lett. **7**, 1237 (1995).

[4] K. D. Choquette, K. M. Geib, C. I. H. Ashby, R. D. Twesten, O. Blum, H. Q. Hou, D. M. Follstaedt, B. E. Hammons, D. Mathes, and R. Hull, Advances in selective wet oxidation of AlGaAs alloys, IEEE J. Sel. Topics Quantum Electron. **3**, 916 (1997).

[5] J. M. Dallesasse and N. Holonyak, Oxidation of al-bearing III-V materials: A review of key progress, J. Appl. Phys. **113**, 051101 (2013).

[6] Karl Welna, Maxime Hugues, Christopher P. Reardon, Liam O'Faolain, Mark Hopkinson, and Thomas F. Krauss, Photonic crystal nanocavities in GaAs/AlGaAs with oxidised bottom cladding, Photonics Nanostruct. Fundam. Appl. **11**, 139 (2013).

[7] Rainer Michalzik, ed., *VCSELs* (Springer, Berlin, Heidelberg, 2013).

[8] R. D. Twesten, D. M. Follstaedt, K. D. Choquette, and R. P. Schneider, Microstructure of laterally oxidized $Al_xGa_{1-x}As$ layers in vertical-cavity lasers, Appl. Phys. Lett. **69**, 19 (1996).

[9] S. Guha, F. Agahi, B. Pezeshki, J. A. Kash, D. W. Kisker, and N. A. Bojarczuk, Microstructure of AlGaAs-oxide heterolayers formed by wet oxidation, Appl. Phys. Lett. **68**, 906 (1996).

[10] P. O. Vaccaro, K. Koizumi, K. Fujita, and T. Ohachi, AlAs oxidation process in GaAs/AlGaAs/AlAs heterostructures grown by molecular beam epitaxy on GaAs (n 11)a substrates, Microelectron. J. **30**, 387 (1999).

[11] Gaël Lafleur, Guilhem Almuneau, Alexandre Arnoult, Henri Camon, and Stéphane Calvez, Anisotropy in the wet thermal oxidation of AlGaAs: Influence of process parameters, Opt. Mater. Express **8**, 1788 (2018).

[12] Pei-Cheng Ku and C. J. Chang-Hasnain, Thermal oxidation of AlgaAs: Modeling and process control, IEEE J. Quantum Electron **39**, 577 (2003).

[13] G. Almuneau, R. Bossuyt, P. Collière, L. Bouscayrol, M. Condé, I. Suarez, V. Bardinal, and C. Fontaine, Real-time in situ monitoring of wet thermal oxidation for precise confinement in VCSELs, Semicond. Sci. Technol. **23**, 105021 (2008).

[14] C. L. Chua, R. L. Thornton, D. W. Treat, and R. M. Donaldson, Anisotropic apertures for polarization-stable laterally oxidized vertical-cavity lasers, Appl. Phys. Lett. **73**, 1631 (1998).

[15] K.-H. Ha, Y.-H. Lee, H.-K. Shin, K.-H. Lee, and S.-M. Whang, Polarisation anisotropy in asymmetric oxide aperture VCSELs, Electron. Lett. **34**, 1401 (1998).

[16] Morten P. Bakker, Ajit V. Barve, Alan Zhan, Larry A. Coldren, Martin P. van Exter, and Dirk Bouwmeester, Polarization degenerate micropillars fabricated by designing elliptical oxide apertures, Appl. Phys. Lett. **104**, 151109 (2014).

[17] Morten P. Bakker, Donald J. Suntrup, Henk Snijders, Tuan-Ahn Truong, Pierre M. Petroff, Dirk Bouwmeester, and Martin P. van Exter, Fine tuning of micropillar cavity modes through repetitive oxidations, Opt. Lett. **38**, 3308 (2013).

[18] N. G. Stoltz, M. Rakher, S. Strauf, A. Badolato, D. D. Lofgreen, P. M. Petroff, L. A. Coldren, and D. Bouwmeester, High-quality factor optical microcavities using oxide apertured micropillars, Appl. Phys. Lett. **87**, 031105 (2005).

[19] D. J. P. Ellis, A. J. Bennett, A. J. Shields, P. Atkinson, and D. A. Ritchie, Electrically addressing a single self-assembled quantum dot, Appl. Phys. Lett. **88**, 133509 (2006).

[20] Stefan Strauf, Nick G. Stoltz, Matthew T. Rakher, Larry A. Coldren, Pierre M. Petroff, and Dirk Bouwmeester, High-frequency single-photon source with polarization control, Nat. Photonics **1**, 704 (2007).

[21] Waldemar Unrau and Dieter Bimberg, Flying qubits and entangled photons, Laser Photonics Rev. **8**, 276 (2013).

[22] Bikash Koley, M. Dagenais, R. Jin, J. Pham, G. Simonis, G. McLane, and Dennis Stone, Kinetics of growth of AlAs oxide in selectively oxidized vertical cavity surface emitting lasers, J. Appl. Phys. **82**, 4586 (1997).

[23] Sheila P. Nabanja, Leslie A. Kolodziejski, and Gale S. Petrich, Lateral oxidation of AlAs for circular and inverted mesa saturable bragg reflectors, IEEE J. Quantum Electron **49**, 731 (2013).

[24] Stephane Calvez, Gaël Lafleur, Alexandre Arnoult, Antoine Monmayrant, Henri Camon, and Guilhem Almuneau, Modelling anisotropic lateral oxidation from circular mesas, Opt. Mater. Express **8**, 1762 (2018).

[25] Carol I. H. Ashby, John P. Sullivan, Kent D. Choquette, K. M. Geib, and Hong Q. Hou, Wet oxidation of AlGaAs: The role of hydrogen, J. Appl. Phys. **82**, 3134 (1997).

[26] M. J. Cich, R. Zhao, Erik H. Anderson, and E. R. Weber, Influence of gas transport on the oxidation rate of aluminum arsenide, J. Appl. Phys. **91**, 121 (2002).

[27] I. Suárez, G. Almuneau, M. Condé, A. Arnoult, and C. Fontaine, Optimal control of AlAs oxidation via digital

alloy heterostructure compositions, J. Phys. D: Appl. Phys. **42**, 175105 (2009).
[28] Nicolaas Godfried Van Kampen, *Stochastic Processes in Physics and Chemistry* (Elsevier, North Holland, Amsterdam, 1992), Vol. 1,
[29] James D. Murray, *Mathematical Biology* (Springer-Verlag, New York, 2002).
[30] R. A. Fisher, The wave of advance of advantageous genes, Ann. Hum. Genet. **7**, 355 (1937).
[31] Andrei N. Kolmogorov, Étude de l'équation de la diffusion avec croissance de laquantité de matière et son application à un problèmebiologique, Bull. Univ. État. Moscou. Sér. Int. A **1**, 1 (1937).
[32] W. Vansaarloos, Front propagation into unstable states, Phys. Rep. **386**, 29 (2003).
[33] Graham R. Dennis, Joseph J. Hope, and Mattias T. Johnsson, XMDS2: Fast, scalable simulation of coupled stochastic partial differential equations, Comput. Phys. Commun. **184**, 201 (2013).
[34] W. K. Burton, N. Cabrera, and F. C. Frank, The growth of crystals and the equilibrium structure of their surfaces, Philos. Trans. R. Soc. A: Math. Phys. Eng. Sci. **243**, 299 (1951).
[35] Robert Luther, Propagation of chemical reactions in space, Elektrochem **12**, 596 (1906).
[36] Stephane Calvez, Gaël Lafleur, Alexandre Larrue, Pierre-Francois Calmon, Alexandre Arnoult, Guilhem Almuneau, and Olivier Gauthier-Lafaye, Vertically coupled microdisk resonators using AlGaAs/AlOx technology, IEEE Photon. Technol. Lett. **27**, 982 (2015).

Correction: A proof change request was not implemented properly in the text after Eq. (3) and has now been set right.